npj | quantum materials

Article

Published in partnership with Nanjing University

https://doi.org/10.1038/s41535-026-00930-3

Robust field-free superconducting diode effect in $FeTe_{0.55}Se_{0.45}$

Check for updates

Peng Dong[1,2,8], Jinghui Wang[1,2,8], Yanjiang Wang[1,2], Jianjun Xiao[1,2], Xiang Zhou[1,2], Hui Xing[3], Kenji Watanabe[4], Takashi Taniguchi[5], Yueshen Wu[1,2] ✉, Yulin Chen[1,2,6], Jinsheng Wen[7] ✉ & Jun Li[1,2] ✉

The superconducting diode effect (SDE), a nonreciprocal phenomenon where the critical supercurrent differs depending on the direction of current flow, is a promising foundation for superconducting logic and memory. Realizing its full potential requires a diode that operates without an applied magnetic field, which generally requires the breaking of both time-reversal and inversion symmetries in the superconducting system. Zero-field SDEs are often observed in heterostructures but remain rare in single materials. Here, we report the observation of a robust, field-free SDE in thin flakes of $FeTe_{0.55}Se_{0.45}$. A sensitive probe of nonreciprocal transport is the emergence of a pronounced second harmonic response near the superconducting transition under zero applied field, with an amplitude comparable to the standard first harmonic signal. The SDE persists at zero field and maintains its polarity under both large positive and negative magnetic fields, exhibiting an even-in-field symmetry that distinguishes it from mechanisms based on finite-momentum pairing or magnetochiral anisotropy. We systematically rule out alternative origins, including device geometry, thermal gradients, chiral domains, and extrinsic magnetic order. Instead, our analysis indicates that local strain/polarization-induced symmetry breaking is a primary factor in generating and enhancing the effect. These results identify iron-based high-temperature superconducting platforms as highly promising candidates for the field-free superconducting diode effect, benefiting from their coexistence of strong intrinsic disorder and superconductivity in a structurally simple form.

The superconducting diode effect (SDE), in which the positive critical current (I_c^+) and the negative critical current (I_c^-) differ[1–4], arises from nonreciprocal transport in superconductors[5,6] and has become one of the central topics in condensed matter physics. The unidirectional transport in single crystals originates from explicit symmetry-breaking mechanisms[4,7–9], including inversion symmetry breaking of the crystal lattice[10]. Alternatively, SDE can also be realized through device structures such as vortex ratchets and rectifiers[11–18], external perturbations like magnetic fields[19], or dynamic superconducting order domains that induce time-reversal symmetry (TRS) breaking[20–25]. The distinctive characteristics inherent to SDE, especially field-free SDE, are highly promising for superconducting physics such as unconventional superconductors[22,26] and for applications in electronic device engineering, including superconducting electronics[27,28] and superconducting-diode-based circuit functionalities[29,30]. To date, field-free SDE has been reported in various superconducting systems, including superconducting superlattice films[11,12,31], asymmetric Josephson junctions[13,19,32–35], superconducting order domains[20,21], and superconducting vortices[19,36]. Importantly, the pursuit of a system exhibiting intrinsic breaking of time-reversal and inversion symmetries serves as an exemplary platform for investigating field-free superconducting diode phenomena.

[1]State Key Laboratory of Quantum Functional Materials, ShanghaiTech University, Shanghai, China. [2]ShanghaiTech Laboratory for Topological Physics & School of Physical Science and Technology, ShanghaiTech University, Shanghai, China. [3]Key Laboratory of Artificial Structures and Quantum Control and Shanghai Center for Complex Physics, School of Physics and Astronomy, Shanghai Jiao Tong University, Shanghai, China. [4]Research Center for Functional Materials, National Institute for Materials Science, National Institute for Materials Science, Tsukuba, Japan. [5]International Center for Materials Nano-architectonics, National Institute for Materials Science, Tsukuba, Japan. [6]Department of Physics, Clarendon Laboratory, University of Oxford, Oxford, UK. [7]National Laboratory of Solid State Microstructures and Department of Physics & Collaborative Innovation Center of Advanced Microstructures and Jiangsu Physical Science Research Center, Nanjing University, Nanjing, China. [8]These authors contributed equally: Peng Dong, Jinghui Wang. ✉e-mail: wuysh@shanghaitech.edu.cn; jwen@nju.edu.cn; lijun3@shanghaitech.edu.cn

Recently, the iron-based superconductor $FeTe_{0.55}Se_{0.45}$ (FTS) has emerged as a prominent candidate for intrinsic topological superconductivity[37] owing to the combination of bulk superconductivity, topological Dirac surface states, and ferromagnetic fluctuations. Crucially, experiments employing angle-resolved photoemission spectroscopy[37,38], spin-polarized tunneling[39,40], nitrogen-vacancy magnetometry[41], surface Kerr effect[42], nano-SQUID imaging[43], and Josephson junction transport[44] have consistently revealed TRS breaking and provided strong evidence of unconventional superconductivity. These findings are consistent with observations of Majorana bound states and robust Yu-Shiba-Rusinov states on the surface of FTS, highlighting its potential as a platform for correlated topological superconductivity and Kondo-driven surface phenomena[45]. FTS lies near a delicate phase boundary involving superconductivity, nematicity, topological states, and ferromagnetism, which can be tuned by slight changes in the Te/Se ratio or interstitial Fe content[46–48]. The superconducting diode phenomenon, serving as a probe for detecting the breaking of spatial inversion and time-reversal symmetries, offers a refined experimental lens to investigate such properties within the superconducting phase.

In this work, we investigated the field-free SDE within the iron-based superconductor FTS flakes. Our findings highlight a 4.6% deviation in critical currents at 10.5 K. Remarkably, the second-harmonic resistance ($R_{xx}^{2\omega}$) demonstrated a distinct non-zero signal at the superconducting transition. This magnitude, on the same order as the first-harmonic resistance (R_{xx}^{ω}), is distinctly different from the magnetochiral anisotropy mechanism. The SDE manifests itself, and stable half-wave rectification has been consistently observed under zero magnetic field. Meanwhile, the SDE maintains its polarization stably under high magnetic fields, and the symmetric response to magnetic fields suggests a mechanism distinct from previously reported field-free SDE. Based on this analysis, we have examined thermal gradients induced by geometric configurations, superconducting chiral domains, magnetic domains, and strain-related factors. The results demonstrate a stronger correlation with strain/polarization, leading us to attribute the observed phenomenon primarily to strain/polarization-induced effects. This field-free SDE phenomenon could streamline the integration of superconducting devices and limit potential interference, thereby offering a promising direction for the development of superconducting electronics utilizing iron-based high-temperature superconductors.

Results

Field-free nonreciprocal transport properties

In Fig. 1a, the crystal structure of FTS is similar to that of FeSe, with inversion symmetry breaking along the out-of-plane direction. The mirror symmetry may be perturbed along the in-plane direction due to the partial substitution of Se atoms by Te atoms. Owing to the van der Waals bonding between FTS layers, the bulk crystal can be readily exfoliated into atomically thin flakes using conventional all-dry exfoliation and transfer techniques.

Following the device fabrication, an optical image of the sample is shown in Fig. 1b, where the total channel length can reach up to 60 μm, making any sub-micron physical influence negligible. As shown in Fig. 1c, the critical temperature is approximately 13 K under low-current excitation. The superconductivity gradually weakens as larger currents are applied. Interestingly, the second-harmonic resistance $R_{xx}^{2\omega}$ signal becomes non-zero at the superconducting transition, even without the application of a magnetic field, as shown in Fig. 1d. Notably, $R_{xx}^{2\omega}$ is comparable in magnitude to the first-harmonic resistance R_{xx}^{ω}, which makes SDE possible. The raw data are shown in Fig. S1. It is important to note that before the device was cooled to its superconducting state, the magnetic field was oscillated to minimize any residual magnetic field to below 1 Oe. Moreover, Figs. S2 and S3 demonstrate a pronounced even-symmetric dependence of the second harmonic resistance on the applied magnetic field, and the orientation of the magnetic field exerts no measurable influence upon the second harmonic resistance.

Field-free SDE

The strong nonreciprocity motivated us to investigate the zero-field SDE using direct current (DC) measurements. Fig. 2a shows the voltage response as a function of DC current at zero magnetic field and various temperatures. Specifically, the solid curve represents the sweep from zero to the positive critical current (I_c^+), while the dashed curve denotes the sweep from zero to the negative critical current (I_c^-). As temperature decreases, both critical currents evolve accordingly, accompanied by a clear asymmetry between the positive and negative bias directions. At 4 K and zero magnetic field, the critical current in the positive direction reaches 0.661 mA, while that in the negative direction is slightly lower at 0.6379 mA. To rigorously rule out any influence from residual magnetic fields, we performed a 180° rotation of the sample, as schematically illustrated in Fig. S4. This procedure has been experimentally validated in previous studies[21,26]. The resulting measurements showed no reversal in the critical current polarity, confirming that remnant magnetic fields have a negligible effect on the observed SDE.

The temperature dependence of the critical current difference between positive and negative bias directions is summarized in Fig. 2b, and the full dataset is provided in Fig. S10. A slight decrease in ΔI_c is observed from 2 K to 10.5 K, followed by a sharp drop to zero at 12 K, indicating the disappearance of the SDE near the superconducting transition temperature. To quantify the strength of the SDE, we define the rectification coefficient η as

$$\eta = \frac{||I_c^+| - |I_c^-||}{|I_c^+| + |I_c^-|} \times 100\%. \quad (1)$$

As shown in Fig. 2b, η remains nearly constant at approximately 2% at low temperatures, increases to around 4.6% with rising temperature, and then rapidly decreases to 0% near the critical temperature. The zero-field SDE was reproducibly observed in 5 devices, with the rectification coefficient η ranging from 0.5% to 4.6%, as illustrated in Fig. S5. Based on experimental results from samples with different thicknesses, the rectification factor η of the SDE exhibits no apparent dependence on material thickness.

A half-wave rectification phenomenon is observed at 4 K under zero applied magnetic field, using a DC current of 0.6575 mA. This particular current value was chosen owing to its asymmetric electrical characteristics, where the positive current sustains the superconducting state, while an equivalent negative current precipitates an instantaneous reversion to normal resistive behavior. This observed polarity-dependent behavior arises from the asymmetric critical currents ($|I_c^+| > |I_c^-|$), manifesting a distinct half-wave rectification effect as demonstrated in Fig. 2c. Furthermore, the rectification effect persists over an extended measurement duration of 1300 s without degradation, strongly indicating that Joule heating is not responsible for the observed current-direction asymmetry in the superconducting response. As illustrated in Fig. S5, a remarkable half-wave rectification effect is sustained for a duration of 3200 s. This long-term stability reinforces the intrinsic nature of the SDE in the studied device, paving the way for applications using iron-based superconductors.

The emergence of field-free nonreciprocal transport and SDE usually occurs in chiral systems. In FTS, the breaking of spatial inversion symmetry along the *c*-axis is inherently satisfied. Furthermore, reported evidence of surface ferromagnetism in FTS indicates the breaking of TRS[42]. In addition to symmetry-based considerations, a few mechanisms have been proposed recently and summarized in Table 1. We then carefully examined these mechanisms below.

Discussion

The most analogous counterpart to our material system is the recently reported thermal-gradient-induced SDE in FeSe crystals[49]. Consequently, we meticulously designed experiments to investigate thermal-gradient effects. As shown in Fig. 3a, the device was transferred onto pre-fabricated electrodes using a dry-transfer process and was subsequently encapsulated with boron nitride (BN) for protection. This was followed by micro-nano fabrication techniques to selectively etch the same sample into both symmetrical and asymmetrical configurations. The symmetric

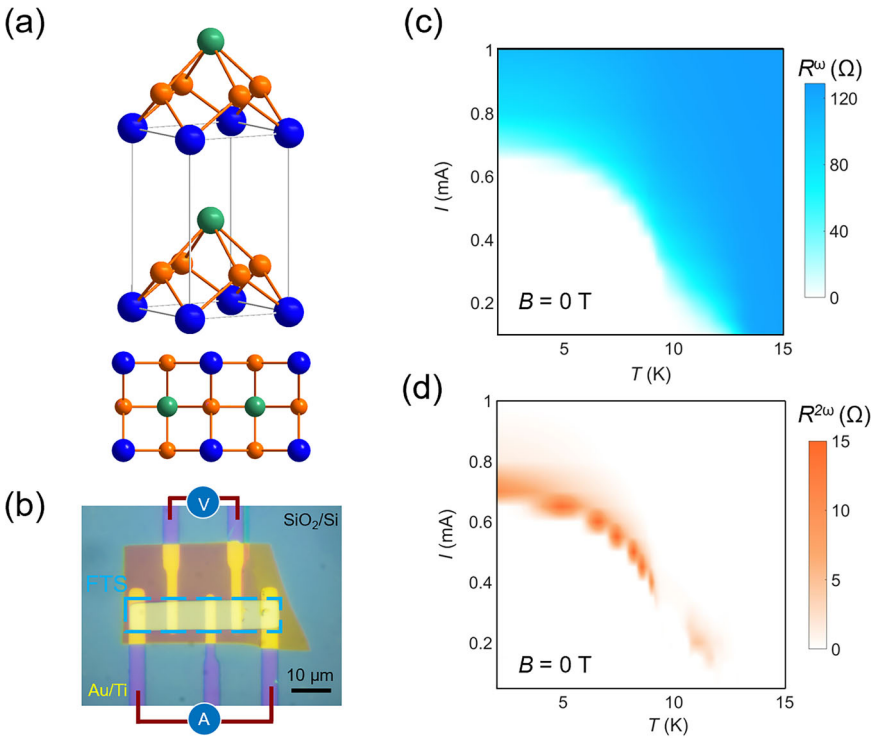

Fig. 1 | Nonreciprocal transport properties in FTS under zero field ($B = 0$ T). **a** Inversion symmetry in the crystal structure of FTS is broken along the *c*-axis. Orange denotes Fe atoms, green signifies Te atoms, and blue represents Se atoms. **b** Optical image of FTS sample. AC or DC current is applied through the electrode positioned at the farthest point to ensure uniform distribution, while the central planar section is designated as the voltage measurement area. **c** The temperature dependence of the first harmonic resistance (R^{ω}_{xx}) under zero field, measured by applying different currents ranging from 50 μA to 1 mA. The zero-resistance state is attained at $T_c^0 = 13$ K under low current excitation. **d** The corresponding second harmonic resistance ($R^{2\omega}_{xx}$) as a function of temperature measured using an AC technique. A pronounced non-zero signal appears at the superconducting transition.

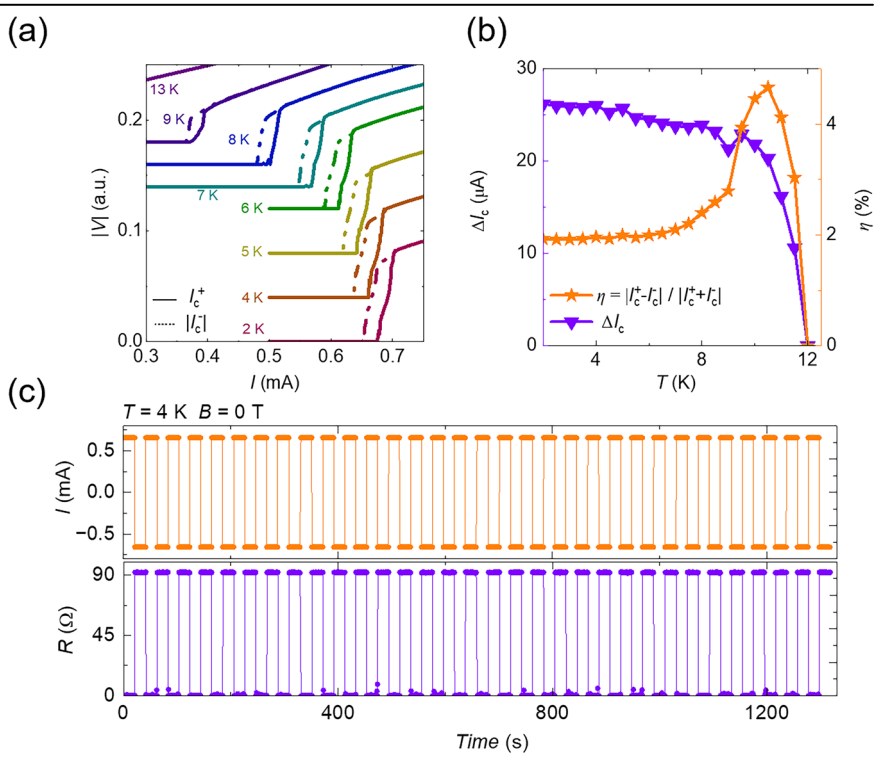

Fig. 2 | Zero-field SDE. **a** The negative side (from 0 mA to −0.8 mA) and positive side (from 0 mA to 0.8 mA) of *I*–*V* curves at different temperatures. A clear difference between the positive and negative critical currents is observed. **b** The disparity in critical current (purple line) diminishes progressively with increasing temperature, whereas the rectification coefficient (orange line) remains invariant at low temperature, undergoes initial amplification to 4.6% as the temperature increases, and ultimately attenuates to zero. **c** Resistance as a function of time under an applied current of ±0.6575 mA at 4 K and zero magnetic field. The half-wave rectification is achieved with high stability and robustness.

device configuration suppresses the formation of thermal gradients, whereas the asymmetric configuration may generate a persistent thermal gradient due to unequal current-terminal contacts, thereby inducing the observed voltage differential (ΔV_{heat}), as illustrated in Fig. 3a. Hence, the thermoelectric potential may be elegantly expressed as: $2\Delta V_{heat} = (I^+R_n + \Delta V_{heat}) - (I^-R_n - \Delta V_{heat})$. Then, we measured the dependence of the rectification coefficient η on the applied out-of-plane magnetic field, as shown in Fig. 3b. Notably, the rectification coefficient exhibits even symmetry with respect to the magnetic field direction, gradually decreasing with increasing field strength and dropping to approximately 0.3% under a 14 T magnetic field. As quantified in Fig. 3c, the negligible voltage difference ΔV_{heat} (on the order of 10^{-5} V) confirms that Joule heating at the terminals is insufficient to account for the observed SDE. For wedge-shaped samples, due to the presence of a significant thermoelectric voltage at the current terminals, both η and ΔV_{heat} exhibited a distinct even-symmetric dependence on the magnetic field, as shown in

Table 1 | A comprehensive summary of field-free superconducting diode systems, detailing the maximum operational temperatures (T_c^{SDE}), the critical magnetic fields of SDE (H_c^{SDE}), rectification coefficients (η), and their origins

Superconductors	T_c^{SDE}	H_c^{SDE}	η	Symmetry	Origin of SDE
Twist trilayer graphene[14]	0.02 K	20 mT	72.9 % (0.02 K)	Odd	Valley imbalance
Superlattice[12]	1.9 K	0.1 T	4.2 % (1.9 K)	Odd	Magnetization
CsV_3Sb_5[21]	3.5 K	1 mT	6.7% (1.4 K)	Odd	Chiral domain
JJs[13,19,33,60]	0.02–77 K	0.022–40 mT	22–60%	Odd/even	Vortex/TRS/polarization
FeSe[49]	10 K	9 T	4.7 % (4 K)	Even	Thermal gradient
BSCCO[26]	72 K	23 mT	22 % (55 K)	Even	Loop current
$PbTaSe_2$[57]	2 K	4 mT	0.2 % (2 K)	Even	Strain
FTS [this work]	12 K	14 T	4.6 % (10.5 K)	Even	Strain/polarization

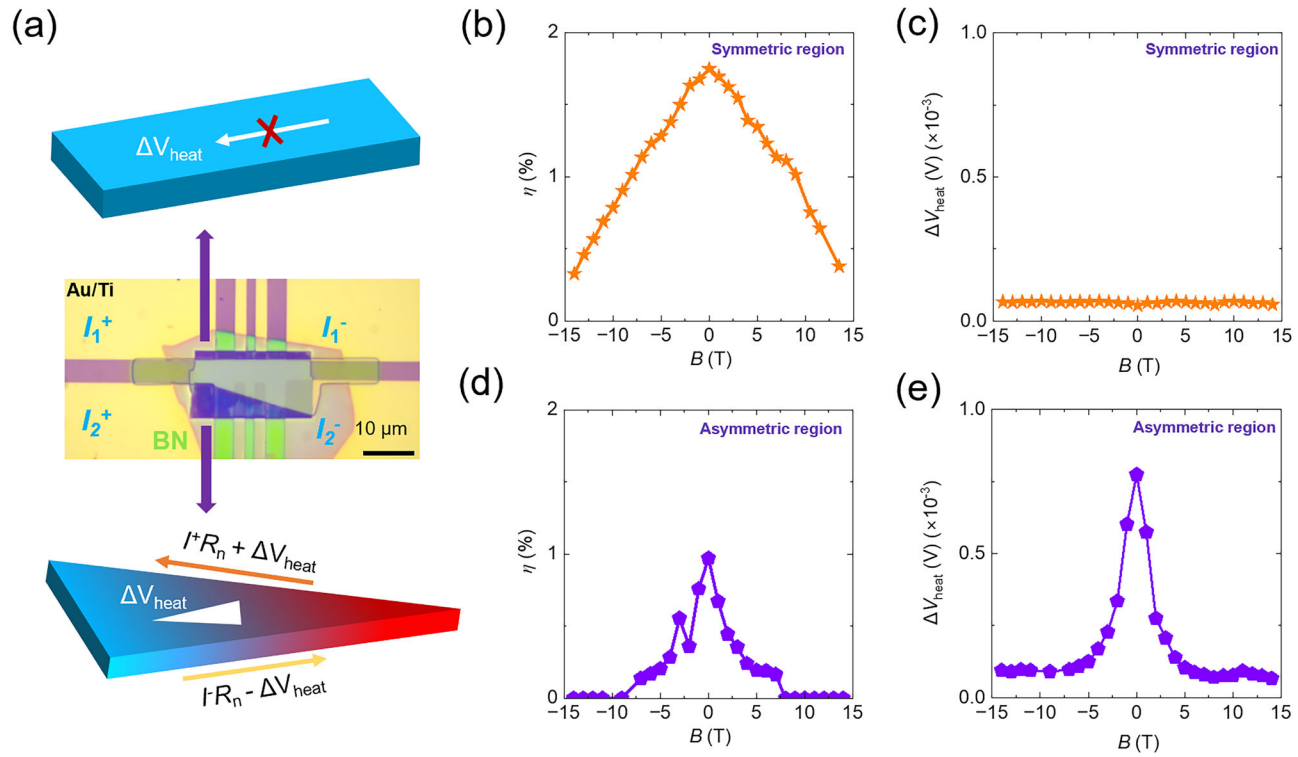

Fig. 3 | The dependence of rectification coefficient (η) and thermoelectric potential (ΔV_{heat}) on magnetic fields in symmetric and asymmetric configurations. a Optical image of symmetric and asymmetric sample with a scale bar denoting 10 μm. The purple regions denote the FTS samples with symmetric and asymmetric geometries, while the yellow regions indicate the pre-patterned electrodes. Illustration of the intrinsic potential voltage difference (ΔV_{heat}) arising from a thermal gradient in the asymmetric specimen. The voltage disparity for equivalent currents of opposite polarity in the normal state manifests as twice the ΔV_{heat}, whereas symmetric geometry exhibits no thermal gradient. **b** The dependence of the rectification coefficient η on the magnetic fields manifests unequivocal even symmetry. **c** The voltage differential (ΔV_{heat}) calculated by $||V_{+0.8mA}| - |V_{-0.8mA}||$ exhibits no discernible dependence on the magnetic field in the symmetric region. **d** The dependence of the rectification coefficient (η) on magnetic fields unequivocally exhibits even symmetry. **e** Compared with the symmetric region, the voltage differential ΔV_{heat} manifests a pronounced even-symmetry characteristic in the asymmetric region.

Fig. 3d, e. Additionally, the thermal gradient remains magnetic-field-independent, whereas the parameter η in all our samples decreases with increasing magnetic field. While thermal gradients have been widely recognized as a key driver of the diode effect in asymmetric structures, we observe a clear SDE in symmetric structures without any intentional thermal gradient. This unambiguously demonstrates that thermal gradients are not the dominant cause of the diode phenomenon in the present superconductor system. All the corresponding raw data are presented in Fig. S6. Our findings further exclude the SDE due to thermal gradients. In addition, we performed systematic current–voltage (I–V) measurements using both forward and backward current sweeps from 2 K to 10 K at 0 T. The results are presented in Fig. S9 and show no measurable hysteresis in any of the measured curves.

Second, vortex ratchets and vortex rectifiers represent an important class of superconducting nonreciprocal transport phenomena, in which asymmetric pinning landscapes convert alternating vortex motion into a net dc response[17,18]. Vortex-pinning-related contributions are generally expected to exhibit a pronounced dependence on magnetic-field polarity and often produce odd-symmetric components in the superconducting diode response. Although the field-free SDE observed here shares some phenomenological similarities with these systems, it exhibits several key differences. In particular, the diode effect in FTS persists at zero applied magnetic field and exhibits an even-symmetric magnetic-field dependence without polarity reversal up to 14 T. Together with the observed robustness against thermal cycling and field-cooling procedures, these characteristics are difficult to reconcile with conventional vortex-ratchet mechanisms.

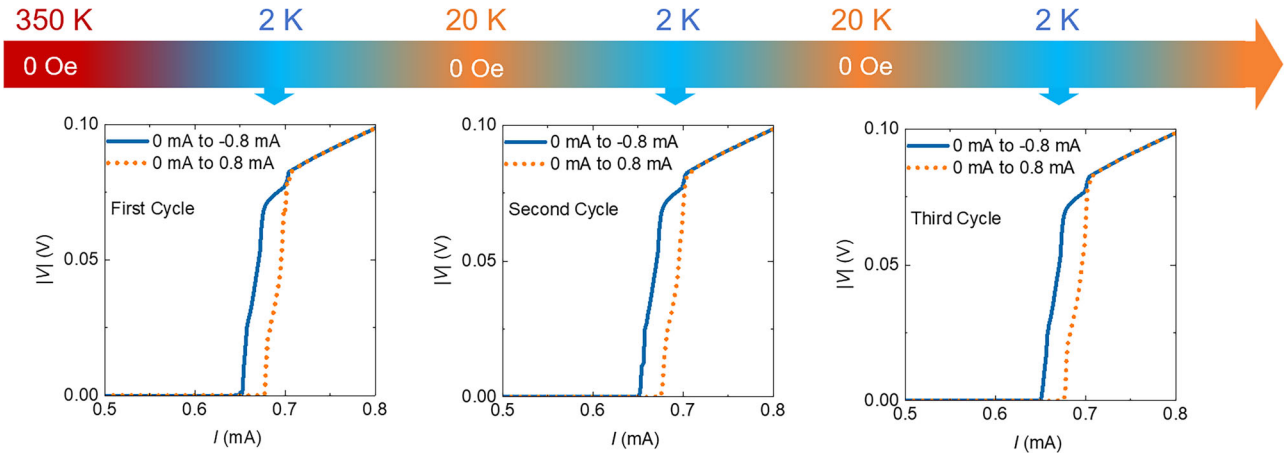

Fig. 4 | Temperature cycling protocol for eliminating chiral domain effects. Repeated temperature cycles from the superconducting state to the normal state were implemented to eliminate potential influences from internal chiral domains.

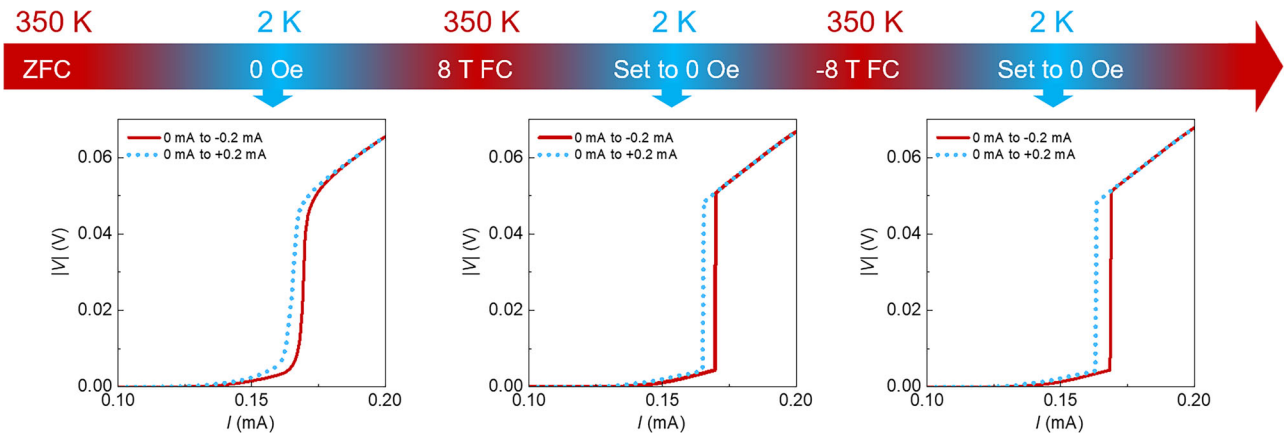

Fig. 5 | Comparison of I–V characteristics under ZFC and FC conditions. The *I*–*V* transport characteristics measured at 2 K under zero magnetic field for samples cooled from 350 K under ZFC or field cooling (FC) at ±8 T show no polarity reversal.

Thirdly, in the single-crystal FTS, translational symmetry remains intact, and the crystal momentum k is well-defined. This ensures that two electrons with momentum k and $-k$ are related through a TRS operation[38]. Consequently, a straightforward symmetry argument implies that SDE cannot occur under TRS. We then consider the effect of TRS breaking. Given the topological properties of FTS, it is conceivable that TRS might be spontaneously broken in its superconducting state. This compound is known to exhibit bulk *s*-wave superconductivity, while its surface demonstrates a topological state that breaks TRS[50,51]. If the SDE were due to superconductivity with broken TRS, we would expect the sign of I_c to switch between positive magnetic field and negative magnetic field, as observed in valley-polarized trilayer graphene[14]. Our measurements show that the field dependence of I_c is symmetric with respect to the field.

On the other hand, superconducting chiral domains with opposite chiralities could affect the SDE. Based on previous observations regarding the thermal modulation of the superconducting chiral domains[21], we systematically warmed samples to the normal state, subsequently restored the oscillating magnetic field to 0 Oe, and then cooled down to the superconducting state. The procedure was repeated for three consecutive cycles, with the *I*–*V* transport characteristics being monitored. As illustrated in Fig. 4, the *I*–*V* properties remained invariant after each thermal cycle, thereby conclusively excluding the presence of chiral domains with broken TRS. This is because domain characteristics, such as asymmetry and inter-domain interactions, are expected to be randomly altered by thermal cycling. Thus, spontaneous formation of chiral domains is not the primary cause of the SDE in this system.

In Fig. S7, despite the similar superconducting critical temperatures, some devices show an upturn before the superconducting transition, whereas others exhibit more metallic behavior. Such variations could be attributed to the common inhomogeneity of single-crystal FTS samples.[52,53], which manifests as local excess Fe ions residing near the Fe sites[54]. Along with the suppression of superconductivity, excess Fe can induce short-range static magnetic order in the samples[55] and spontaneous TRS breaking, which may contribute to the emergence of the SDE. In our devices, the presence of local magnetic moments can be inferred from the sign changes of the magnetoresistance resulting from the competition between Drude-like transport and Kondo-like scattering[56].

To eliminate the influence of inhomogeneous magnetic domains, the sample was initially cooled from 350 K to 2 K under zero-field cooling (ZFC), followed by measurement of *I*–*V* characteristics. Subsequently, it was warmed to 350 K and field-cooled to 2 K under both 8 T and −8 T magnetic fields (FC), with *I*–*V* characteristics measured at each condition, as shown in Fig. 5. Nevertheless, the results revealed no polarity reversal, indicating that inhomogeneous magnetic domains do not contribute to the observed SDE behavior.

The field-free SDE and the even-in-field rectification coefficient resemble those reported in earlier studies, such as $PbTaSe_2$[57], BSCCO[26], where strain-induced polarization or loop currents could induce the zero-field diode effect. Concomitant evidence suggests that localized strain induced by internal polarization in FTS modulates its superconducting

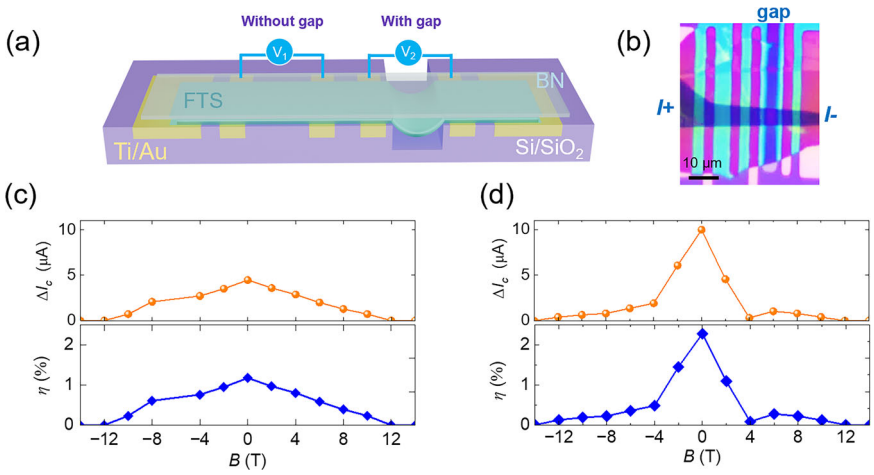

Fig. 6 | Comparative analysis of rectification coefficients η with and without localized strain. **a** Schematic illustration of the sample structure in the strain application experiment. The right electrode underwent additional photolithography and RIE to create a gap approximately 1.3 μm deep. Mechanical strain was induced in the periphery of the specimen through compressive deformation during the transfer process. **b** The depiction of the specimen, wherein a gap has been marked out. **c** The dependence of ΔI_c and η on the magnetic field in the region without a gap. The region of localized strain exhibits an even-symmetry dependence for the rectification coefficient with respect to the magnetic field. **d** The dependence of ΔI_c and η on the magnetic field in the gapped region. In contrast, the stressed region demonstrates an even-symmetry characteristic in the rectification coefficient, accompanied by a 1% enhancement.

properties[58]. This interpretation proposes that a zero-field SDE does not necessarily rely on broken TRS[13,57,59]. Conventionally, the SDE is considered forbidden in the presence of TRS, as discussed above. However, introducing electron-electron interactions allows for SDE even without breaking TRS. Theoretical considerations suggest that electron correlation effects lead to a charging effect in the polar direction, resulting in an asymmetric dependence on current direction and, consequently, a zero-field SDE[59].

The strain experiment was designed using a specialized electrode configuration, as depicted in Fig. 6(a). During electrode fabrication, reactive ion beam etching (RIE) was employed to achieve a 27 nm profile, followed by the deposition of a 29 nm Ti/Au film. The key distinction is that the left voltage terminal has a pristine SiO_2 surface, whereas the right terminal contains a 1.3 μm recess etched by RIE. Upon transferring the sample onto the electrodes, strain gradients were naturally generated near the edges, thereby enabling a concurrent comparative analysis of strain effects on the SDE in regions with and without significant applied strain. Figure 6b depicts the optical photograph of the sample. Intriguingly, in the regions without strain in Fig. 6c, we observed that ΔI_c has no sign reversal and the rectification coefficient η exhibited a distinct even-symmetric dependence on the magnetic field. Similarly, in the regions with applied strain, ΔI_c exhibits a conspicuous enhancement, yet no sign reversal is observed. The rectification coefficient η maintains an even-symmetric characteristic and exhibits a 1% enhancement, indicating that strain can influence the rectification coefficient of SDE in Fig. 6d. We therefore speculate that variations in local strain could contribute to the device-to-device variation in rectification coefficient.

In Table 1, we summarized the highest temperature (T_c^{SDE}) and magnetic field (H_c^{SDE}) maintaining the SDE, together with the proposed origins reported in previous studies. Notably, the SDE polarity in our sample remains robust under magnetic fields up to 14 T. Most reports of strain-induced field-even SDEs have reported H_c^{SDE} values of only several dozen to hundreds of Gauss. For chiral- or magnetic-domain-induced SDE, the polarity may change within several tens of Gauss. Thermal gradient-induced SDE causes local heating and substantial cooling power consumption in integrated superconducting logic circuits. Consequently, our system's high-field resilience offers significant advantages for stable device operation, particularly in environments with unavoidable magnetic fluctuations.

To conclude, we investigated the emergence of field-free nonreciprocal transport phenomena in the iron-based superconductor FTS. Notably, a second harmonic resistance ($R_{xx}^{2\omega}$) of comparable magnitude to the first harmonic resistance (R_{xx}^{ω}) was observed. Our experimental results demonstrate that the disparity in critical currents is approximately 4.6% of the average value at 10.5 K. The symmetric response of ΔI_c and the rectification coefficient η indicate a mechanism distinct from those of previously reported zero-field SDEs. The SDE polarity remains robust under magnetic fields up to 14 T. Through meticulously designed experiments, we have systematically ruled out factors such as geometry-induced thermal gradients, chiral domains, and magnetic domains, ultimately attributing the observed phenomenon to the influence of localized strain. Strain may serve as the origin of broken inversion symmetry or induced polarization, while strong correlations further amplify nonlinear charge transport and nonreciprocal responses, collectively giving rise to a zero-field SDE. This occurrence of field-free SDE could simplify the integration of superconducting devices. The coexistence of strong intrinsic disorder and superconductivity allows us to probe the stability of the SDE in iron-based high-temperature superconductors.

Methods

Crystal growth

High-quality single crystals of FTS were grown using the horizontal Bridgman method. The stoichiometric raw materials (99.99% Fe, 99.99% Te, 99.99% Se) of nominal composition were mixed well and sealed in an ampoule under vacuum. The ampoule was then heated up and slowly cooled down to room temperature in a tube furnace. Each grown crystal weighs about 10 g and has a shiny cleaved surface.

Device fabrication

The sample is initially exfoliated onto a silicon wafer cleaned by oxygen plasma treatment. Subsequently, a conventional transfer technique employing BN is utilized to encapsulate the sample. Through a combination of photolithography and etching processes, the specimen is patterned into a well-defined geometry. Further lithographic patterning is then performed on the structured sample. The etching depth of BN in the electrode regions is carefully controlled until the FTS surface is exposed, ensuring optimal ohmic contact formation.

Transport measurements

We first characterized the nonreciprocity of superconductivity at zero magnetic field using a standard low-frequency (73 Hz) lock-in technique in a four-probe measurement geometry. This frequency is sufficiently far from common environmental noise sources associated with 50/60 Hz power lines and their harmonics, and the second-harmonic response exhibits no systematic frequency dependence across this range in Fig. S8. All electrical measurements were carried out in a Quantum Design Physical Property Measurement System. The first and second harmonic resistances were defined as $R_{xx}^{\omega} = \sqrt{2}V_{xx}^{\omega}/I$ and $R_{xx}^{2\omega} = \sqrt{2}V_{xx}^{2\omega}/I$, where I denotes the amplitude of the sinusoidal AC current, and V_{xx}^{ω} and $V_{xx}^{2\omega}$ are the amplitudes of the first and second harmonic voltage signals measured by the lock-in amplifier. A phase shift of $\pi/2$ was applied to the

second harmonic component to compensate for the intrinsic phase difference.

Data availability

The datasets generated and/or analyzed during the current study are not publicly available due to their large volume but are available from the corresponding author on reasonable request.

Received: 4 February 2026; Accepted: 18 July 2026;
Published online: 02 August 2026

References

1. Mao, Y., Yan, Q., Zhuang, Y.-C. & Sun, Q.-F. Universal spin superconducting diode effect from spin-orbit coupling. *Phys. Rev. Lett.* **132**, 216001 (2024).
2. Nadeem, M., Fuhrer, M. S. & Wang, X. The superconducting diode effect. *Nat. Rev. Phys.* **5**, 558 (2023).
3. Jiang, K. & Hu, J. Superconducting diode effects. *Nat. Phys.* **18**, 1145 (2022).
4. Yuan, N. F. & Fu, L. Supercurrent diode effect and finite-momentum superconductors. *Proc. Natl. Acad. Sci. USA* **119**, e2119548119 (2022).
5. Hoshino, S., Wakatsuki, R., Hamamoto, K. & Nagaosa, N. Nonreciprocal charge transport in two-dimensional noncentrosymmetric superconductors. *Phys. Rev. B* **98**, 054510 (2018).
6. Guo, C. et al. Switchable chiral transport in charge-ordered kagome metal CsV_3Sb_5. *Nature* **611**, 461 (2022).
7. Dong, P. et al. Nonreciprocal superconductivity at Ti_2O_3/GaN interface. *APL Quantum* **2**, 016114 (2025).
8. Yerin, Y., Drechsler, S.-L., Varlamov, A. A., Cuoco, M. & Giazotto, F. Supercurrent rectification with time-reversal symmetry broken multiband superconductors. *Phys. Rev. B* **110**, 054501 (2024).
9. Cheong, S. W., Talbayev, D., Kiryukhin, V. et al. Broken symmetries, non-reciprocity, and multiferroicity. *npj Quantum Mater.* **3**, 19 (2018).
10. Bauriedl, L. et al. Supercurrent diode effect and magnetochiral anisotropy in few-layer $NbSe_2$. *Nat. Commun.* **13**, 4266 (2022).
11. Ando, F. et al. Observation of superconducting diode effect. *Nature* **584**, 373 (2020).
12. Narita, H. et al. Field-free superconducting diode effect in noncentrosymmetric superconductor/ferromagnet multilayers. *Nat. Nanotechnol.* **17**, 823 (2022).
13. Wu, H. et al. The field-free Josephson diode in a van der Waals heterostructure. *Nature* **604**, 653 (2022).
14. Lin, J.-X. et al. Zero-field superconducting diode effect in small-twist-angle trilayer graphene. *Nat. Phys.* **18**, 1221 (2022).
15. Lyu, Y.-Y. et al. Superconducting diode effect via conformal-mapped nanoholes. *Nat. Commun.* **12**, 2703 (2021).
16. He, J. et al. Proximity-induced superconducting diode effect in antiferromagnetic Mott insulator α-$RuCl_3$. *Adv. Funct. Mater.* **35**, 2504056 (2025).
17. Villegas, J. E. et al. A superconducting reversible rectifier that controls the motion of magnetic flux quanta. *Science* **302**, 1188–1191 (2003).
18. Cerbu, D. et al. Vortex ratchet induced by controlled edge roughness. *N. J. Phys.* **15**, 063066 (2013).
19. Ghosh, S. et al. High-temperature Josephson diode. *Nat. Mater.* **23**, 612 (2024).
20. Wan, Z. et al. Unconventional superconductivity in chiral molecule–TaS_2 hybrid superlattices. *Nature* **632**, 69 (2024).
21. Le, T. et al. Superconducting diode effect and interference patterns in kagome CsV_3Sb_5. *Nature* **630**, 64 (2024).
22. Zinkl, B., Hamamoto, K. & Sigrist, M. Symmetry conditions for the superconducting diode effect in chiral superconductors. *Phys. Rev. Res.* **4**, 033167 (2022).
23. Wu, Y. et al. Nonreciprocal charge transport in topological kagome superconductor CsV_3Sb_5. *npj Quantum Mater.* **7**, 105 (2022).
24. He, J. J., Tanaka, Y. & Nagaosa, N. The supercurrent diode effect and nonreciprocal paraconductivity due to the chiral structure of nanotubes. *Nat. Commun.* **14**, 3330 (2023).
25. Xie, Y. M., Isobe, H. & Nagaosa, N. Nonreciprocal nonlinear responses in moving charge density waves. *npj Quantum Mater.* **9**, 82 (2024).
26. Qi, S. et al. High-temperature field-free superconducting diode effect in high-T_c cuprates. *Nat. Commun.* **16**, 531 (2025).
27. Castellani, M. et al. A superconducting full-wave bridge rectifier. *Nat. Electron.* **8**, 417 (2025).
28. Devoret, M. H. & Schoelkopf, R. J. Superconducting circuits for quantum information: an outlook. *Science* **339**, 1169 (2013).
29. Wang, H. et al. Quantum superconducting diode effect with perfect efficiency above liquid-nitrogen temperature. *Nat. Phys.* **22**, 47–53 (2026).
30. Hu, G., Han, Y., Guo, H. et al. Polarity-reversible zero-field diode effect in van der Waals ferromagnetic Josephson junction for logic operation. *Adv. Mater.* **38**, e13434 (2026).
31. Hou, Y. et al. Ubiquitous superconducting diode effect in superconductor thin films. *Phys. Rev. Lett.* **131**, 027001 (2023).
32. Baumgartner, C. et al. Supercurrent rectification and magnetochiral effects in symmetric Josephson junctions. *Nat. Nanotechnol.* **17**, 39 (2022).
33. Zhao, S. F. et al. Time-reversal symmetry breaking superconductivity between twisted cuprate superconductors. *Science* **382**, 1422 (2023).
34. Pal, B. et al. Josephson diode effect from Cooper pair momentum in a topological semimetal. *Nat. Phys.* **18**, 1228 (2022).
35. Zhang, E. et al. Observation of edge supercurrent in topological antiferromagnet $MnBi_2Te_4$-based Josephson junctions. *Sci. Adv.* **11**, eads8730 (2025).
36. Gutfreund, A. et al. Direct observation of a superconducting vortex diode. *Nat. Commun.* **14**, 1630 (2023).
37. Lv, B., Qian, T. & Ding, H. Angle-resolved photoemission spectroscopy and its application to topological materials. *Nat. Rev. Phys.* **1**, 609 (2019).
38. Zhang, P. et al. Observation of topological superconductivity on the surface of an iron-based superconductor. *Science* **360**, 182 (2018).
39. Wang, D. et al. Evidence for Majorana bound states in an iron-based superconductor. *Science* **362**, 333 (2018).
40. Machida, T. et al. Zero-energy vortex bound state in the superconducting topological surface state of Fe(Se,Te). *Nat. Mater.* **18**, 811 (2019).
41. McLaughlin, N. J. et al. Strong correlation between superconductivity and ferromagnetism in an Fe-chalcogenide superconductor. *Nano Lett.* **21**, 7277 (2021).
42. Farhang, C. et al. Revealing the origin of time-reversal symmetry breaking in Fe-chalcogenide superconductor $FeTe_{1-x}Se_x$. *Phys. Rev. Lett.* **130**, 046702 (2023).
43. Lin, Y. et al. Direct observation of quantum anomalous vortex in Fe(Se,Te). *Phys. Rev. X* **13**, 011046 (2023).
44. Qiu, G. et al. Emergent ferromagnetism with superconductivity in Fe(Te,Se) van der Waals Josephson junctions. *Nat. Commun.* **14**, 6691 (2023).
45. Chatzopoulos, D. et al. Spatially dispersing Yu-Shiba-Rusinov states in the unconventional superconductor $FeTe_{0.55}Se_{0.45}$. *Nat. Commun.* **12**, 298 (2021).
46. Katayama, N. et al. Investigation of the spin-glass regime between the antiferromagnetic and superconducting phases in $Fe_{1+y}Se_xTe_{1-x}$. *J. Phys. Soc. Jpn.* **79**, 113702 (2010).
47. Reiss, P. et al. Collapse of metallicity and high-T_c superconductivity in the high-pressure phase of $FeSe_{0.89}Te_{0.11}$. *npj Quantum Mater.* **9**, 73 (2024).
48. Islam, K. R. & Chubukov, A. Unconventional superconductivity near a nematic instability in a multi-orbital system. *npj Quantum Mater.* **9**, 28 (2024).
49. Nagata, U. et al. Field-free superconducting diode effect in layered superconductor FeSe. *Phys. Rev. Lett.* **134**, 236703 (2025).

50. Roppongi, M. et al. Topology meets time-reversal symmetry breaking in $FeSe_{1-x}Te_x$ superconductors. *Nat. Commun.* **16**, 6573 (2025).
51. Hanaguri, T., Niitaka, S., Kuroki, K. & Takagi, H. Unconventional *s*-wave superconductivity in Fe(Se,Te). *Science* **328**, 474 (2010).
52. He, X. et al. Nanoscale chemical phase separation in $FeTe_{0.55}Se_{0.45}$ as seen via scanning tunneling spectroscopy. *Phys. Rev. B* **83**, 220502 (2011).
53. Wen, J., Xu, G., Gu, G., Tranquada, J. & Birgeneau, R. Interplay between magnetism and superconductivity in iron-chalcogenide superconductors: crystal growth and characterizations. *Rep. Prog. Phys.* **74**, 124503 (2011).
54. Liu, X. et al. X-ray diffuse scattering study of local distortions in $Fe_{1+x}Te$ induced by excess Fe. *Phys. Rev. B* **83**, 184523 (2011).
55. Xu, Z. et al. Disappearance of static magnetic order and evolution of spin fluctuations in $Fe_{1+\delta}Se_xTe_{1-x}$. *Phys. Rev. B* **82**, 104525 (2010).
56. Yang, Y. et al. Possible Kondo scattering and its signature in Seebeck coefficient in topological superconductor $Fe_{1+y}Se_{0.55}Te_{0.45}$. *J. Magn. Magn. Mater.* **564**, 170126 (2022).
57. Liu, F. et al. Superconducting diode effect under time-reversal symmetry. *Sci. Adv.* **10**, eado1502 (2024).
58. Zhao, H. et al. Nematic transition and nanoscale suppression of superconductivity in Fe(Te,Se). *Nat. Phys.* **17**, 903 (2021).
59. Morimoto, T. & Nagaosa, N. Nonreciprocal current from electron interactions in noncentrosymmetric crystals: roles of time reversal symmetry and dissipation. *Sci. Rep.* **8**, 1 (2018).
60. Zeng, X.et al. Large superconducting diode effect driven by edge states in twisted iron-chalcogenide Josephson junctions. arXiv:2510.00595 (2025).

Acknowledgements

This work was supported by the National Key Projects for Research and Development of China (Grants No. 2022YFA1603903, 2021YFA1400400, and 2024YFA1409200), the National Natural Science Foundation of China (Grants No. 62571327, 92565112, 92565305, 12434005, 12225407), the Natural Science Foundation of Shanghai (Grants No. 25ZR1402374, 25ZR1402368, and 25ZR1401252), the Science and Technology Commission of Shanghai Municipality, the Shanghai Leading Talent Program of Eastern Talent Plan, State Key Laboratory of Micro-nano Engineering Science (Grant No. MES202603), and the Double First-Class Initiative Fund of ShanghaiTech University. Growth of hexagonal BN crystals was supported by the Elemental Strategy Initiative conducted by the MEXT, Japan, Grant Number JPMXP0112101001, JSPS KAKENHI Grant Number JP20H00354, and A3 Foresight by JSPS. We gratefully acknowledge Prof. Xiao Lin of Westlake University and Prof. Baiqing Lv of the Tsung Dao Lee Institute at Shanghai Jiao Tong University for their valuable comments and suggestions.

Author contributions

P.D. and J.H.W. contributed equally to this work. P.D., Y.S.W. and J.L. designed the research. J.H.W. grew the single crystals of $FeTe_{0.55}Se_{0.45}$. K.W. and T.T. grew the single crystals of h-BN. P.D. fabricated the samples and performed the electrical transport measurements. Y.J.W. and J.J.X. assisted with device fabrication. P.D., J.H.W., X.Z., H.X., Y.S.W., J.S.W., Y.L.C. and J.L. contributed to data analysis. P.D., J.H.W., Y.S.W. and J.L. wrote the paper.

Competing interests

The authors declare no competing interests.

Additional information

Supplementary information The online version contains supplementary material available at https://doi.org/10.1038/s41535-026-00930-3.

Correspondence and requests for materials should be addressed to Yueshen Wu, Jinsheng Wen or Jun Li.

Reprints and permissions information is available at http://www.nature.com/reprints

Publisher's note Springer Nature remains neutral with regard to jurisdictional claims in published maps and institutional affiliations.

Open Access This article is licensed under a Creative Commons Attribution-NonCommercial-NoDerivatives 4.0 International License, which permits any non-commercial use, sharing, distribution and reproduction in any medium or format, as long as you give appropriate credit to the original author(s) and the source, provide a link to the Creative Commons licence, and indicate if you modified the licensed material. You do not have permission under this licence to share adapted material derived from this article or parts of it. The images or other third party material in this article are included in the article's Creative Commons licence, unless indicated otherwise in a credit line to the material. If material is not included in the article's Creative Commons licence and your intended use is not permitted by statutory regulation or exceeds the permitted use, you will need to obtain permission directly from the copyright holder. To view a copy of this licence, visit http://creativecommons.org/licenses/by-nc-nd/4.0/.

© The Author(s) 2026